Cloud Type and Macrophysical Property Retrieval Using Multiple Remote Sensors

ZHIEN WANG AND KENNETH SASSEN

Department of Meteorology, University of Utah, Salt Lake City, Utah

(Manuscript received 2 October 2000, in final form 16 March 2001)

ABSTRACT

A cloud detection algorithm based on ground-based remote sensors has been developed that can differentiate among various atmospheric targets such as ice and water clouds, virga, precipitation, and aerosol layers. Standard cloud type and macrophysical properties are identified by combining polarization lidar, millimeter-wave radar, infrared radiometer, and dual-channel microwave radiometer measurements. These algorithms are applied to measurements collected during 1998 from the Atmospheric Radiation Measurement Program Cloud and Radiation Test Bed site in north-central Oklahoma. The statistical properties of clouds for this year are presented, illustrating how extended-time remote sensing datasets can be converted to cloud properties of concern to climate research.

1. Introduction

Understanding the role of clouds in the global hydrological cycle and energy budget is one of the important goals for current climate research programs. To achieve this goal requires the collection and analysis of extensive observations with sets of surface- and satellite-based remote sensors covering long time periods, and the development of models that properly couple cloud processes with the other major components of the climate system (Stokes and Schwartz 1994; Asrar and Dozier 1994; Rossow and Schiffer 1999). How to combine the observations of different ground and satellite-based sensors optimally to provide the necessary cloud information has yet to be resolved.

A variety of active and passive sensors have traditionally been relied on to obtain cloud information from both the ground and space. Active (lidar and radar) sensors provide vertically resolved cloud information; passive sensors generally measure path-integrated cloud properties. However, information on the vertical distribution of clouds can be retrieved from passive sensor measurements using some algorithms (Stubenrauch et al. 1999; Wang et al. 1996). Polarization lidar and millimeter-wave radar are two important active remote sensors used in cloud studies, and when used together the different working wavelengths allow them to complement each other. Although lidar cannot penetrate thick low and midlevel clouds because of strong optical attenuation, most mid- and high-level clouds can be accurately sampled. Radar, on the other hand, can penetrate low clouds to detect many middle and high clouds. Thus combining lidar and radar measurements provides more reliable cloud boundary and thickness data (Uttal et al. 1995; Clothiaux et al. 2000). Different passive sensors may also have complementary capabilities. Visible and infrared (IR) radiometers provide path-integrated optical properties, whereas microwave radiometers (MWR) provide path-integrated water vapor and liquid water content information. To provide complete retrievals of cloud microphysical and macrophysical properties, we need to develop algorithms that optimally combine the measurements from an ensemble of appropriate remote sensors.

In this paper, algorithms to retrieve cloud macrophysical properties, which include boundary, thickness, phase, type, and precipitation information, by combining ground-based lidar, millimeter-wave radar, IR radiometer, and MWR measurements are described. Such instrument ensembles are available at growing numbers of ground-based sites, such as the Facility for Atmospheric Remote Sensing (FARS) at the University of Utah (Sassen et al. 2001) and the Department of Energy Atmospheric Radiation Measurement (ARM) Program Cloud and Radiation Test Bed (CART) sites (Stokes and Schwartz 1994).

In section 2 of this paper, a lidar cloud detection algorithm is introduced. Combining lidar and radar measurements to derive cloud boundaries is discussed in section 3. In section 4, an algorithm to classify clouds into standard categories is presented. Cloud-phase determination using the lidar linear depolarization ratio δ is discussed in section 5. The algorithms are applied to measurements collected at the Southern Great Plains (SGP) CART site in Oklahoma during 1998, and the resulting statistics of cloud macrophysical properties are

Corresponding author address: Zhien Wang, University of Utah, 135 S 1460 E 819 WBB, Salt Lake City, UT 84112-0110.
E-mail: zwang@met.utah.edu

© 2001 American Meteorological Society

Unauthenticated | Downloaded 05/29/24 05:42 AM UTC

TABLE 1. Characteristics of the instruments at the SGP CART site used in this study.

Instrument	Wavelength/ frequency	Temporal/spatial resolution	Observed or derived quantity
Raman lidar	0.355 μm	60 s, 39 m	Cloud extinction, backscattering coefficient, depolarization
MPL	0.5235 μm	60 s, 300 or 30 m	Altitude of clouds
MWR	23.8 GHz, 31.4 GHz	60 s, column integrated	Brightness temperature, LWP, water vapor path
IR thermometer	9.9–11.5 μm	60 s, column integrated	Brightness temperature, downward IR radiance
MMCR	34.86 GHz	10 s, 45-m range gate	Reflectivity factor, Doppler velocity, Doppler width

presented in section 6. In Table 1, we list the general characteristics of the five remote sensing systems from the SGP CART site used in this study.

2. The lidar cloud detection algorithm

a. Background

The definition of cloud base is influenced by various research requirements. The definition adopted by the U.S. National Weather Service is based on the rotating-beam ceilometer, which defines cloud base as the height at which the backscattered signal reaches its maximum value (Eberhard 1986). This definition obviously locates the cloud-base height somewhat inside clouds. Platt et al. (1994) defined cloud-base altitude as that altitude above which hydrometers exist and can be detected to be liquid droplets, ice particles, or rain. To generate correct cloud overlap rate statistics (Barker et al. 1999) for radiation budget studies, we adopt this general definition, except we separate virga and precipitation from the potentially more radiatively important suspended cloud particles. The same definition of cloud base applies to cloud top.

As described by Platt et al. (1994), during the Experimental Cloud Lidar Pilot Study three basic methods were applied to the determination of cloud boundaries from lidar measurements: the differential zero-crossing method (Pal et al. 1992), the threshold method (Winker and Vaughan 1994), and a quantitative approach based on the clear-air scattering assumption (Sassen and Cho 1992).

The first two algorithms are related because they both discriminate the change in lidar signal from the gradually decreasing backscatter with altitude below cloud base to the typically sharp increase in backscatter just above cloud base. Both algorithms need careful tuning to reject small backscatter enhancements caused by noise and aerosol returns. The third method avoids some of these problems but is most useful in the upper troposphere, where aerosol returns are generally negligible. Recently, Young (1995) used an alternative cloud detection algorithm for optically thin clouds. In addition, Campbell et al. (1998) and Clothiaux et al. (1998) developed algorithms for the detection of hydrometer returns in micropulse lidar (MPL) data. These latter algorithms can be classified as threshold methods.

To detect clouds from lidar measurements, algorithms have to distinguish between signal changes due to random noise and signal increases from aerosols and those due to clouds. For mixed-phase midlevel clouds, a considerable depth of virga often exists below the dense generating cloud layers. As mentioned above, the ability to distinguish source clouds from virga and precipitation is very important for generating more accurate cloud statistics (Barker et al. 1999). There unfortunately is currently no universal algorithm or collection of algorithms that is suitable for all situations, has the ability to handle signal quality, and can differentiate among various targets such as clouds, virga, and aerosols. The presentation of a more general cloud detection algorithm to separate cloud from noise and aerosol signals is one of the purposes of this paper.

b. A general cloud detection algorithm

Strong negative and positive slopes in the lidar backscatter signal are typically observed in the presence of clouds. For the algorithm described here, we start from the characteristics of the lidar signal, such as in the differential zero-crossing and threshold methods, but also take into account the underlying physical differences among cloud and aerosol layers, and noise effects. The algorithm includes five steps, which are discussed in more detail in Wang (2000).

The first step is to calculate the slope and quality of the signal, as well as the standard deviation σ of the background noise level using a range-uncorrected averaged vertical profile. The data-averaging procedure depends on an examination of signal quality, such as the noise level and σ, which can vary from case to case. The variation of the signal $S(R_i)$, which characterizes the quality of the signal and increases with increasing noise, is defined by

$$S(R_i) = \frac{\sum_{j=i-n/2}^{i+n/2} \text{abs}\{\ln[P(R_j)] - a - bR_j\}}{\sum_{j=i-n/2}^{i+n/2} \ln[P(R_j)]}, \quad (1)$$

Unauthenticated | Downloaded 05/29/24 05:42 AM UTC

where P is power, R_i is range or altitude, and a and b are the coefficients from fitting $P(R_{i-n/2}), \ldots, P(R_i), \ldots, P(R_{i+n/2})$ to the linear function $\ln[P(R_i)] = a + bR_i$, where b is the slope of the signal. The number of points n used for fitting depends on the vertical resolution of the lidar system. In our algorithm, the slope and $S(R_i)$ are calculated for the whole profile, and a minimum reliable signal $P_{\min}$ is defined for lidar data with a given signal-averaging scheme. If the signal lies below $P_{\min}$, it is considered to be unsuitable for analysis. We find that $P_{\min}$ should generally be larger than 3σ.

The second step is to examine the lidar signal upward from the ground and record possible layers and their properties, such as the height of layer base, peak, and top; the ratio of the peak signal to that of the layer base T; and the maximum negative slope D within each layer. Any layer identified could be a cloud, aerosol, or a noise peak. Layer base corresponds to where the signal starts to increase in terms of the positive signal slope, and layer top is where the signal returns to either the molecular backscattering or the noise level.

For middle or high clouds, the following principle is used to determine the layer base: the initial increase at the base must be 3σ or greater, and the signal cannot decrease to the base level within a short range interval, depending on the vertical resolution of the sensor. For high-vertical-resolution systems, we find that at least three points of continuous increase should be used to select a layer base as in Sassen and Cho (1992), but this clearly may not be possible for low-resolution systems. For some cases involving low and middle clouds, this principle can find a cloud base that is actually due to precipitation, virga, or aerosol below the cloud. Because of strong attenuation in low clouds and the $1/R^2$ effect in range-uncorrected signals at low levels, a strong signal increase above cloud base does not always happen in the presence of subcloud precipitation, virga, or aerosol. In these situations, it is helpful to use range-corrected signals for low-cloud detection, or the strong negative slope due to overwhelming attenuation in dense clouds can be used to trigger a cloud-base identification.

After detecting a layer base, the height at which the signal is reduced below either the base signal or an estimate of the signal due to clear-air return at the corresponding height (calibrated below the layer base by assuming no aerosol is present) is determined. Once this height is found, the layer-top height can be determined. The layer top will be located at the altitude at which the signal slope returns to the slope of the clear-sky signal or the magnitude of the signal drops below $P_{\min}$. If the signal-to-noise ratio at the layer top is acceptable, then the maximum negative slope within 500–800 m above the layer top is found. The layer-top height is searched again starting from the height of maximum negative slope provided that the maximum negative slope is smaller (more negative) than a certain threshold and the signal quality is still acceptable. This tuning step mainly addresses the case of clouds with multiple signal peaks. If a weak layer is detected within 50 m above a strong layer and the signal strength is acceptable, the weak layer is included with the strong layer. This method processes any combination of cloud and aerosol layers.

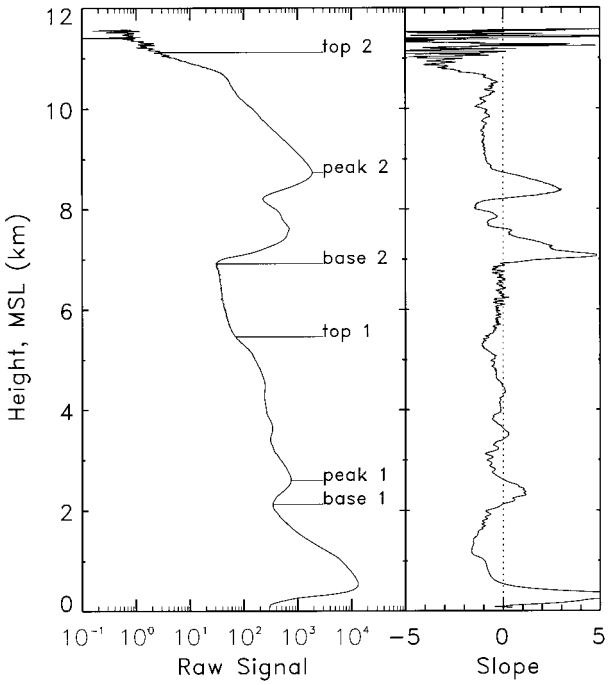

FIG. 1. An example of the second step in the algorithm, which detects layer structure from the lidar signal. MSL is the height above mean sea level.

An example of this step is illustrated in Fig. 1. Two layers are detected in this profile. (Note that the peak structure below 1 km is due to the overlap of the lidar receiving and transmitting systems.) At bases 1 and 2, a signal increase is clearly indicated by the positive slope. The heights of top 1 and top 2 are determined according to the change of slope. At top 1, the signal slope returns to the slope of air return (~ -0.8), and at top 2, the slope of signal changes from negative to positive because the signal displays too much noise.

The third step is to distinguish a cloud from noise or an aerosol layer. Aerosols are often stratified in the troposphere and can cause features similar to those of clouds in lidar backscattering. The main difference between cloud and aerosol layers that we exploit is the different magnitudes of the extinction and backscattering coefficients. If the effects of range and cloud attenuation are neglected, the ratio T is defined as

$$T = \frac{P_{\text{peak}}}{P_{\text{base}}} \approx \frac{\beta_{\text{peak}}}{\beta_{\text{base}}}, \tag{2}$$

where β_{peak} and β_{base} are the backscattering coefficients at layer peak and base, respectively. If molecular scattering is assumed to contribute most to β_{base}, this ratio

Unauthenticated | Downloaded 05/29/24 05:42 AM UTC

approximates the magnitude of particle backscattering at the altitude of the peak signal. Because most clouds are considerably more dense than aerosols at the same altitude, and thin cirrus clouds only occur at relatively high altitudes, a preselected value for this ratio can distinguish these layers. For a 0.355-μm-wavelength, high-resolution lidar, a T value of 4 for $R \leq 5$ km and 1.5 for $R > 5$ km effectively distinguishes cloud from aerosol layers at the SGP CART site. However, dense low clouds sometimes show small T because of strong hydrometeor attenuation and/or in the presence of aerosol or precipitation below cloud. For this case, D is also a good parameter for discriminating clouds from aerosols or noise. In our experience, if $D < -7$ and $R > 0.8$ km, a cloud layer typically is present in a lidar return. If T and D are below their thresholds, the target is regarded as an aerosol layer or is due to noise. These preselected values change, however, with the wavelength and vertical resolution of the lidar system because the attenuation and backscattering coefficients of air molecules, aerosols, and clouds have different wavelength dependencies, and low-resolution systems detect smoother cloud signals than high-resolution systems. Note that $S(R)$ is an excellent indicator of the effect of noise (Wang 2000). If $S(R)$ is larger than a given threshold, but T and D are too small, it is highly likely that the detected layer is generated by noise, and such layers are rejected.

The fourth step is to judge whether the cloud top is an actual top or an *effective* top height. In many cases involving optically thick clouds, lidars are unable to penetrate the cloud layer, and thus the detected cloud top is not the true top height. If the signal above cloud top is below $P_{\min}$ with a zero mean slope and strong attenuation (according to the negative slope) is detected within the cloud, the cloud top is likely an effective top. If the signal above cloud top is larger than $P_{\min}$ and has a negative slope approximately equal to the slope of the molecular signal, the cloud top represents the actual top height.

The fifth step is to distinguish cloud base from virga base for mixed-phase or drizzle-producing clouds. Although the lidar signal from virga or drizzle also increases with height, its slope is typically much smaller than that at cloud base because of the different magnitudes of extinction and backscattering coefficients. Moreover, dense water clouds can attenuate the lidar signal very rapidly (<200–300 m), which is indicated by a strong negative slope. The strong positive slope from virga to cloud and the strong negative slope aloft in water clouds from attenuation provide important information for distinguishing cloud-base from virga-base altitudes. An example of FARS ruby (0.694 μm) lidar signal with the signal slope from a cloud layer with virga extending below is presented in Fig. 2. A strong increase in slope from the virga to the cloud layer is clearly present, followed by a strong negative slope. The first strong increase in slope is selected as the cloud base, and the layer base is defined as the virga base. For the case shown in Fig. 2, there is about a 500 m difference between these two bases.

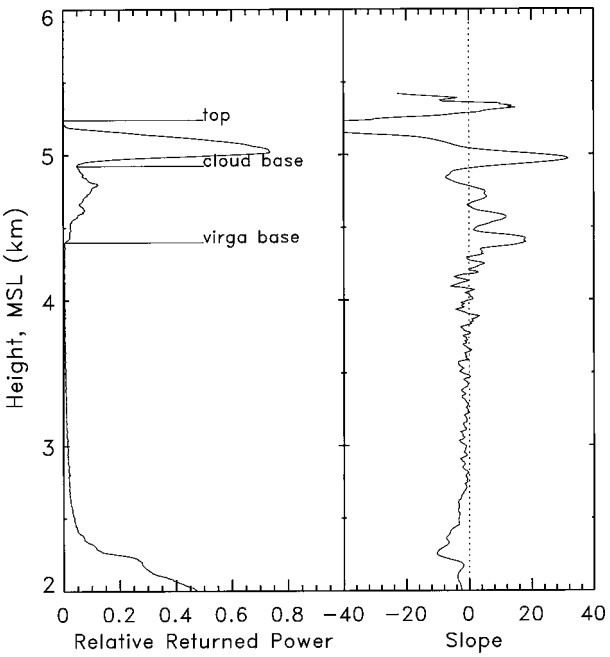

FIG. 2. An example of distinguishing cloud-base height from virga-base height.

From these five steps, the following properties are output for each layer: layer base, layer peak, cloud base, cloud top, and a flag for cloud top (indicating actual or effective top). If the lidar system provides depolarization data, phase information of the cloud layer can also be provided by δ values (see section 5). This general algorithm can also be used for millimeter-wave radar signal analysis with some modifications. Because there is no air return in the radar signals, and virga–cloud boundaries are generally not distinguishable without Doppler spectra, then only the first three steps are considered for radar measurements. However, $P_{\min}$ and other threshold values should be tuned for radar according to the noise level of the data. Nonetheless, to derive more complete information regarding cloud boundaries, the lidar and radar measurements need to be combined (see section 3).

c. Discussion

Differences clearly exist among various lidar algorithms in their ability to determine cloud top, analyze multilayer clouds, and distinguish clouds from aerosols and noise. Even if a lidar detects a molecular return above a cloud, most algorithms cannot correctly determine the cloud-top height. The algorithm of Pal et al. (1992), for example, only determines the apparent cloud-top height R_t by the criterion requiring that the lidar signal at R_t be less than or equal to the signal at

Unauthenticated | Downloaded 05/29/24 05:42 AM UTC

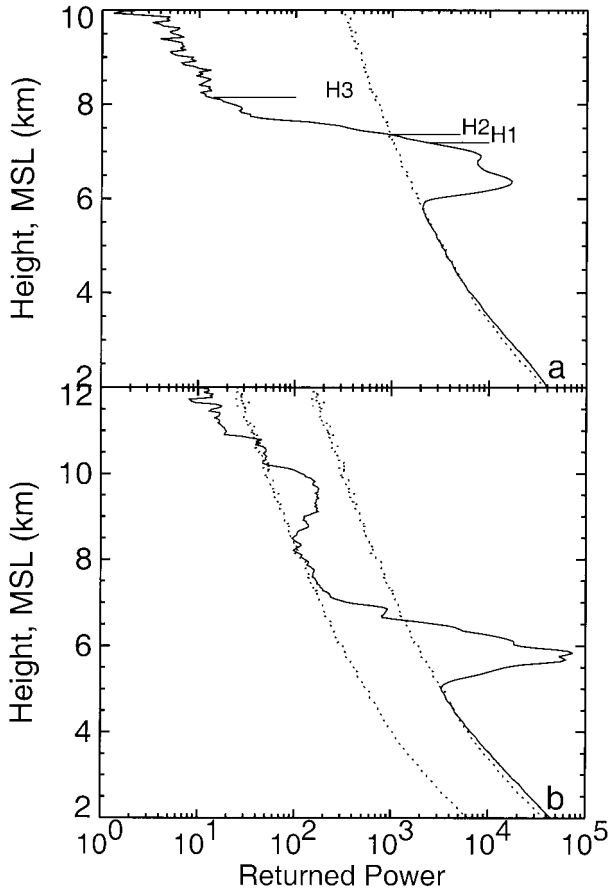

FIG. 3. Examples of backscattered lidar signals. In (a) and (b) dashed lines are the clear-sky returns normalized by the signal below the cloud.

the cloud base. It is obvious that the apparent cloud-top height H1 is typically lower than the actual cloud top H3 in Fig. 3a. The cloud-top height H2 determined by using the attenuated lidar scattering ratio (Winker and Vaughan 1994) is also biased negatively. Clothiaux et al. (1998) determined the significance of the power return from particles by using thresholds defined according to the ratio *r*, which is approximately equal to the attenuated lidar scattering ratio minus one. Thus it has a problem similar to using the attenuated lidar scattering ratio. As shown above, the actual cloud top is better determined by using the signal slope if an air return is detected above the cloud. The differences in cloud-top heights among the different methods are also affected by cloud optical thickness and the vertical profile of the extinction coefficient.

Figure 3b shows the backscattered lidar signal profile for two-layer clouds. It indicates that various algorithms will display different abilities to detect upper cloud layers (~8.5–10.8 km) because of the attenuation produced by lower clouds (~5.1–7.1 km). Threshold algorithms based on the attenuated lidar scattering ratio or the estimated cloud backscatter coefficient have potential problems in properly determining the upper cloud layers, because their attenuated backscattering coefficients can fall below the molecular backscattering normalized to below the lower clouds. However, algorithms using slope information (Pal et al. 1992; current algorithm) can detect the upper cloud layers (if they are detectable by the lidar system), because the attenuation of lower clouds only affects the magnitude of upper-layer cloud signal and not the slope of the cloud signal.

As an example, Figs. 4a,b show the lidar scattering ratios and cloud boundaries determined from CART Raman lidar measurements (Goldsmith et al. 1998) using the new approach, where the red and black dots indicate cloud top and cloud base, respectively. The results around 1900 (all times are UTC) on the first day clearly show that the new approach is able to detect the multilayer clouds. The other parts in Fig. 4 will be explained later.

The thresholds in most algorithms are selected to eliminate the effect of noise, but the effects of aerosols are not generally considered. Thus various algorithms have different capabilities in differentiating aerosol layers from clouds. In the current algorithm, the parameter *T*, the peak-signal–to–base-signal ratio, is introduced to distinguish these targets. To illustrate this approach, the cumulative frequency between *T* and T_{max} (~50) is plotted as a function of *T* for *T* between 1 and 8 in Fig. 5; the dashed lines in Fig. 5 indicate the thresholds currently in use. All Raman lidar measurements collected in 1998 at the SGP CART site are used for this analysis. Note that there is a large portion of detected layers with small *T*. If these layers are counted as clouds, it would result in a considerable systematic error in the cloud statistics. As shown in Fig. 5b, the result is not very sensitive to the threshold when the cloud base is below 5 km, because clouds are much thicker than aerosols in this altitude range. On the other hand, the result for high-cloud detection is sensitive to the threshold because of the occurrence of subvisual and thin cirrus. The threshold of 1.5 is a reasonable value because the optical depth of a 1-km-thick cirrus with a peak lidar scattering ratio of 1.5 at 10-km altitude is about 0.05, and most detected layers with small *T* are only a few hundred meters in depth. From the cumulative frequency value between the current threshold and T_{max}, we can see that about 40% of the detected layers are rejected by the current thresholds. Among these rejected layers, about 50% appear above or below a cloud layer.

3. Cloud boundaries from lidar and cloud radar measurements

Cloud boundaries and thicknesses are basic macrophysical properties with important radiative implications. Although lidars are generally sensitive enough to detect any cloud in the troposphere, they often cannot penetrate through thick clouds to reach cloud top (Clothiaux et al. 2000). Because of the λ^{-4} dependence (where

Unauthenticated | Downloaded 05/29/24 05:42 AM UTC

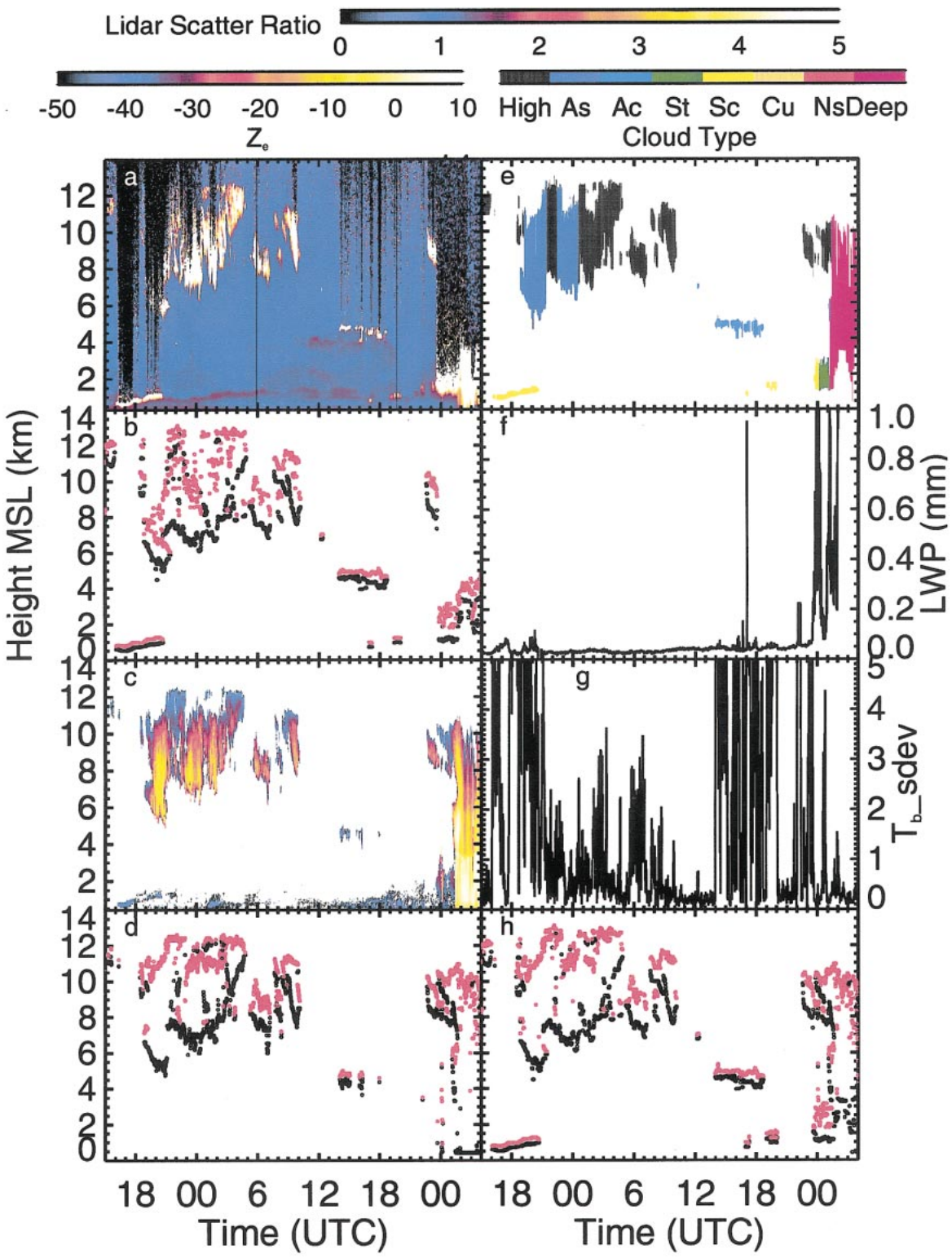

FIG. 4. An example of cloud detection and classification: (a) lidar scattering ratio from Raman lidar measurements, (b) cloud boundaries from Raman lidar measurements, (c) radar reflectivity factor from an MMCR, (d) cloud boundaries derived from radar measurements, (e) results of cloud classification, (f) LWP (mm) measured by MWR, (g) the standard deviation of T_b, and (h) cloud boundaries by combining Raman lidar and MMCR measurements.

Unauthenticated | Downloaded 05/29/24 05:42 AM UTC

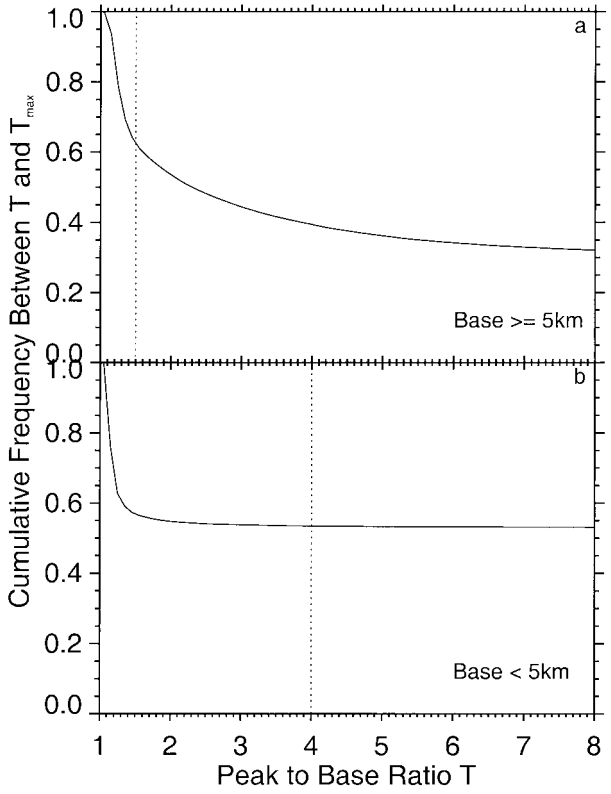

FIG. 5. Cumulative frequency between T and T_{max} as a function of T: (a) layer bases $\geq$5 km and (b) layer bases $<$5 km. Layers with T smaller than the threshold (indicated with a dashed line) are counted as an aerosol layer or noise.

λ is wavelength) in the Rayleigh backscattering coefficient, K-band (35 GHz) and W-band (94 GHz) radars are widely used for cloud research. Signals from advanced research-grade radars, such as the CART millimeter-wave cloud radar (MMCR, see Table 1), however, are often contaminated by virga, precipitation, or even insects, which are not necessarily radiatively important in comparison with clouds. The MMCR also fails to detect some clouds that contain small particles—for example, altocumulus and thin cirrus clouds. Properly combining lidar and radar measurements, then, is a powerful tool to provide more reliable cloud boundary data.

The following principles are used to combine lidar and radar measurements. First, radar data are analyzed to provide radar-echo cloud base and top, as well as precipitation information. If the effective radar reflectivity factor Z_e (mm^6 m^{-3}) in the first two gates of the radar echo is larger than a given threshold, precipitation may be present. Currently, -10 dBZ_e is selected as the threshold to identify precipitation for the MMCR. Then, in the second step, the lidar data are analyzed for cloud boundaries, and radar precipitation information is used in the analysis. The lidar algorithm described above is used to determine cloud boundaries if there is no precipitation detected by the radar. If precipitation is indicated, cloud base is selected at the last signal increase before overwhelming attenuation occurs in the lidar signal, which indicates the dense portion of the source cloud. If virga is present, the radar echo base is lower than the lidar cloud base, which is determined by using the slope and magnitude of the lidar signal as previously discussed.

The third step is to combine the lidar and radar results to give the best estimate of the cloud boundaries. Cloud-base height is always determined from available lidar measurements. However, cloud top is determined either from the lidar or radar data, depending on cloud optical thickness. If the cloud is too thick for the lidar to penetrate, a radar echo top is assigned instead of cloud-top height, because it likely has a bias that makes it lower than the actual cloud top in most clouds. For a situation in which the cloud droplets or ice crystals are too small for the radar to detect, cloud base and top can only be derived from lidar measurements. If multilayer clouds are present and the lower layer blocks the lidar, radar echo base and top are assigned as the cloud base and top of the upper layer or layers.

Two checks are implemented to reduce the possible effects of insect scattering on low-level cloud detection using MMCR data. First, we use the criteria $Z_e(i + 1) > 0.1$ and $R(i) < 3.0$ km, or $Z_e(i + 1) - Z_e(i) > 0.02$ and $Z_e(i + 1) > 0.1$ to separate low-level cloud and precipitation from insect signals. These criteria come from an analysis of radar signals when other evidence shows bug contamination to have been present. Another approach to identifying contamination from insects is to use vertical Z_e profiles–based adiabatic model simulations (Mace and Sassen 2000). Second, we use the low-level clouds detected by lidar or ceilometer to reject incorrect radar low-level cloud detection.

Because we use a variety of measurements to determine the cloud-base and -top heights under different situations, flags are assigned to these variables. In our current scheme, the cloud-base flag has a value of 0 or 1, which indicates that the cloud base is determined by lidar signal or radar echo, respectively. The cloud-top flag can have values of 0, 1, or 2, which represent lidar effective top, lidar actual top, or radar echo top, respectively.

An example of the combined results is shown in Fig. 4h, where the cloud boundaries from Raman lidar and MMCR data are shown in Figs. 4b,d. When there is precipitation, the radar echo base is biased to be lower than the lidar cloud base as shown in the final few hours in Figs. 4b,d. Comparing the cloud tops, we can see the limitation of lidar to detect the top of optically thick clouds because of strong attenuation. It is easy to find where the MMCR has failed to detect thin cirrus and midlevel supercooled water clouds by comparing Fig. 4c with Fig. 4a. This example clearly demonstrates the necessity of combining lidar and cloud radar measurements to provide the best cloud detection and to derive more reliable cloud boundaries.

Unauthenticated | Downloaded 05/29/24 05:42 AM UTC

TABLE 2. Characteristic cloud features for the major cloud types derived from numerous studies. Our cloud-type identification algorithm is based on many of these characteristics. Heights are above ground level. Horiz. and Vert. dim. stand for horizontal and vertical dimensions, respectively.

Cloud class		Cloud features
High cloud	Base	>7.0 km
	Rain	No
	Horiz. dim.	10^3 km
	Vert. dim.	Moderate
	LWP	=0
As	Base	2.0–7.0 km
	Rain	None
	Horiz. dim.	10^3 km, homogeneous
	Vert. dim.	Moderate
	LWP	~0, dominated by ice
Ac	Base	2.0–7.0 km
	Rain	Virga possible
	Horiz. dim.	10^3 km, inhomogeneous
	Vert. dim.	Shallow or moderate
	LWP	>0
St	Base	0–2.0 km
	Rain	None or slight
	Horiz. dim.	10^2 km, homogeneous
	Vert. dim.	Shallow
	LWP	>0
Sc	Base	0–2.0 km
	Rain	Drizzle or snow possible
	Horiz. dim.	10^3 km, inhomogeneous
	Vert. dim.	Shallow
	LWP	>0
Cu	Base	0–3.0 km
	Rain	Drizzle or snow possible
	Horiz. dim.	1 km, isolated
	Vert. dim.	Shallow or moderate
	LWP	>0
Ns	Base	0–4.0 km
	Rain	Prolonged rain or snow
	Horiz. dim.	10^3 km
	Vert. dim.	Thick
	LWP	>0
Deep convective clouds	Base	0–3.0 km
	Rain	Intense shower of rain or hail possible
	Horiz. dim.	10 km
	Vert. dim.	Thick
	LWP	>0

4. Cloud classification

Because of the different radiative forcings of various cloud types (Hartmann et al. 1992; Chen et al. 2000), classifying clouds into categories based on type is an important task for cloud remote sensing and global cloud climatological studies. Algorithms based on different cloud spectral, textural, and physical features have been developed for cloud classification from satellites (Welch et al. 1992; Tovinkere et al. 1993; Bankert 1994; Luo et al. 1995; Rossow and Schiffer 1999). The International Satellite Cloud Climatology Project (ISCCP) approach (Rossow and Schiffer 1999) uses the combination of cloud-top pressure and cloud optical depth to classify clouds into either cumulus (Cu), stratocumulus (Sc), stratus (St), altocumulus (Ac), altostratus (As), nimbostratus (Ns), cirrus, cirrostratus, or deep convective clouds. Table 2 shows the basic features of these different cloud types (World Meteorological Organization 1956; Parker 1988; Uddstrom and Gray 1996; Moran et al. 1997). However, with more long-term ground-based remote sensing cloud studies underway, algorithms to classify cloud type using this approach are a necessity. Duchon and O'Malley (1999) studied the possibility of classifying clouds according to ground-based solar flux measurements. Their results show an accuracy of classification below 50%. Williams et al. (1995) developed an algorithm to classify precipitating clouds into either stratiform, mixed stratiform, convective, and deep or shallow convective clouds using 915-MHz wind profile data.

In this study, we present a new algorithm to classify clouds into either St, Sc, Cu, Ns, Ac, As, deep convective, or high cloud by combining ground-based active and passive remote sensing data. The class of high cloud includes cirrus, cirrocumulus, and cirrostratus, and deep convective cloud represents cumulus congestus and cumulonimbus.

Unauthenticated | Downloaded 05/29/24 05:42 AM UTC

a. Measurements used for cloud classification

We classify clouds by using vertical and horizontal cloud properties, the presence or absence of precipitation, liquid water path (LWP), and downward IR brightness temperature T_b. Details of our approach are given in Wang (2000). Vertically pointing lidar and radar provide a time series of vertical cloud profiles, and the vertical and horizontal extents of clouds represent important information for differentiating cloud types. In addition to active remote sensing data, IR radiometer and MWR measurements are also incorporated into our scheme. Infrared radiometers measure the total T_b of the atmospheric column from gases and clouds combined. Although the T_b due to the cloud can be estimated from this and supplementary data, the standard deviation of T_b, which is calculated from high-frequency ($\sim$0.05 Hz) measurements, is found to be more useful for identifying cloud type. For clear sky, T_b changes very slowly with time, primarily in accordance with column water vapor changes. However, it changes in a different manner for different types of clouds because of the fundamental horizontal inhomogeneities and fractional coverage of clouds and the change of cloud-base height with time. LWP retrieved from MWR measurements is another important layer-integrated cloud property. For water clouds, LWP can be approximately related to cloud optical depth by using the effective radius of the cloud droplets.

As an example, LWP, the standard deviation of T_b, and the combined lidar–radar cloud boundaries as a function of time are illustrated in Figs. 4f–h. The significant amount of LWP observed indicates the appearance of water clouds or liquid precipitation. However, the accuracy of LWP retrieved from MWR measurements can be poor for low-LWP clouds. The residual error or ''theoretical accuracy'' of LWP using a statistical retrieval method is about 0.03 mm in current CART data, about 10 times the sensitivity or noise limit (0.003 mm) of the MWR. The retrieval method may also result in a significant clear-sky LWP bias, as shown in Fig. 4f.

b. Methodology

Role-based classification methods, which assign different threshold values to characteristic parameters, are simple and easy-to-use methods, but the results are sensitive to the selection of the thresholds. Instead of using Boolean logic, the proper use of fuzzy logic can improve the results of cloud classification (Penaloza and Welch 1996). The approach of using neural networks to classify cloud type in satellite imagery has shown recent success (Welch et al. 1992; Bankert 1994). The network is trained on selected spectral, textural, and physical features associated with expertly labeled samples. The trained network is subsequently applied to unknown cloud samples. However, these new classification techniques cannot guarantee better performance, which depends on how properly designed the classifier is and the selection of features (Tovinkere et al. 1993).

The rule-based classification method is selected in this study for its simplicity. We use the following strategy to classify clouds. First, cloud masks (from cloud boundaries) are used to find a cloud cluster according to their persistence in the horizontal (i.e., time) and vertical directions. To consider better the real situation, a 2-min break is allowed in a cluster. If a detected cloud cluster originally lasts less than 1 h, it will be forced to extend at the same height region until it is equal to or longer than 1 h, because we use cloud mean properties within a 1-h window to classify clouds. Therefore, a cloud cluster permits spatially broken cloud fields.

Once a cloud cluster is found, the mean cloud-base and -top heights, as well as the occurrence of precipitation, are determined. If precipitation occurs during the period, the cloud cluster is divided into three subperiods: before, during, and after the precipitation. The clouds in the precipitation period will be classified as either Ns, Ac, Sc, or deep convective cloud according to the base and top heights and how long the precipitation lasts (see Table 2). A nonprecipitating cloud cluster is passed to a high, middle, or low classifier according to its mean cloud base.

Noting that the low, middle, and high classifier scheme uses a 1-h window, to measure cloud-base changes and cloud brokenness quantitatively the following parameters are defined:

$$f_{\text{time}} = \frac{t_{\text{cloud cover}}}{t_{\text{window}}}, \qquad \text{Ratio} = \frac{\sigma_{\text{base}}}{\text{Mean cloud depth}},$$

$$\text{Base}_{\text{dif}} = \frac{1}{N}\sum_{i=1}^{N} \text{abs}(\text{base}_i - \text{base}_{\text{mean}}), \quad \text{and}$$

$$\text{Ratio1} = \frac{\text{Base}_{\text{highest}} - \text{base}_{\text{lowest}}}{\text{Mean cloud depth}}, \tag{3}$$

where $t_{\text{cloud cover}}$ is the total cloud coverage time measured in the time window t_{window}, and σ_{base} is the standard deviation of cloud base within the time window. The fractional time of cloud cover overhead is measured by f_{time}, and the absolute and relative changes of cloud base are measured by Base_{dif}, Ratio, and Ratio1. This algorithm is tuned and applied to the observations at the SGP CART site for 1998 (see below). As an example, Fig. 4e provides the classification results for the cloud returns shown in Figs. 4a,c.

c. Comparisons with visual observations

It must be recognized that the identification of cloud type from remote sensing and standard visual observations is based on fundamentally different approaches. Human observers classify clouds based on their visual appearance and approximate cloud height. The result of visual observations depends on the knowledge and ex-

Unauthenticated | Downloaded 05/29/24 05:42 AM UTC

TABLE 3. Contingency table showing comparison of cloud type derived from the algorithm vs cloud type from human visual observations for Jan 1998.

		Algorithm								
		High	As	Ac	St	Sc	Cu	Ns	Deep	Clear
Obs	High	39	2	3	0	2	1	1	0	7
	As	10	37	1	0	0	0	0	0	0
	Ac	13	1	15	4	1	0	0	0	7
	St	0	1	0	55	12	0	12	0	1
	Sc	0	0	0	8	13	0	0	0	2
	Cu	0	0	0	0	0	0	0	0	0
	Ns	0	0	0	0	0	0	20	0	0
	Deep	0	0	0	0	0	0	0	0	0

perience of the operator, and there are priorities for reporting different cloud types if there are multiple cloud types present. In contrast, cloud types determined from ground-based remote sensors are based on measured physical cloud properties. So, we may hope to see an overall agreement, but some differences in the results will likely be present.

Visual observations are taken by the SGP CART central facility operator, who records cloud type and height using the World Meteorological Organization cloud scene code for each quadrant of the sky, and ($\sim$30°) overhead at the beginning of each hour during most daylight hours. Note that when the operator reported no clouds present, no comparisons were made, and for overcast situations, we did a comparison only up to the overcast layer. If the reported cloud code represents an occurrence of multiple cloud types, and the algorithm-derived cloud type is one of these clouds, then we consider the two to be in agreement.

A comparison of cloud type from near-overhead visual observations and our algorithm is presented in Tables 3 and 4. The main differences result from two factors. The first is due to the use of an objective threshold for high cloud height in the algorithm, and the second is due to the incorrect estimation of cloud height by the observer. For example, we found cases in which the observer reported a cloud height of 5.5 km, whereas the lidar and radar measured a cloud-base height at about 10 km. Visual observations have difficulty in properly estimating cloud thickness, which can also result in some differences in cloud type. In the two months selected for comparison, there is an approximately 8% chance that the observer reported small amounts of cloud and the lidar and radar did not detect any cloud. The overall agreement is about 64% between visual observations and the results of the algorithm in these two months, but is improved to about 70% if we exclude the cases in which the lidar and radar did not detect clouds in the zenith.

5. Cloud-phase determination using polarization lidar

Thermodynamic phase is an important cloud property, and cloud-phase discrimination is a basic step for cloud research because we must apply different parameters or algorithms to derive the microphysical properties of clouds. ISCCP simply uses temperature to divide clouds into categories of water clouds and ice clouds. However, cloud phase is not exactly determined by temperature, and therefore we need more information for cloud-phase discrimination. Sassen (1991) shows that lidar linear depolarization ratios δ are a unique parameter for cloud-phase discrimination. That is, according to cloud phase, δ changes with height in characteristic ways.

For pure water clouds, δ values are essentially zero near cloud base and then tend to increase with height because of multiple scattering, depending on the design of the lidar receiver. For mixed-phase clouds with virga, there are generally large δ below the source cloud because of precipitating ice crystals and because of low δ and strong backscattering aloft where water droplets

TABLE 4. Contingency table showing comparison of cloud type derived from the algorithm vs cloud type from human visual observations for May 1998.

		Algorithm								
		High	As	Ac	St	Sc	Cu	Ns	Deep	Clear
Obs	High	33	8	0	0	0	0	0	0	4
	As	16	23	0	0	2	0	1	0	0
	Ac	7	5	49	0	3	1	1	2	10
	St	0	0	1	7	0	0	4	0	0
	Sc	0	4	9	0	14	8	3	2	1
	Cu	0	0	2	0	0	31	0	0	9
	Ns	0	0	0	0	0	0	6	1	0
	Deep	0	0	1	0	0	0	0	4	0

Unauthenticated | Downloaded 05/29/24 05:42 AM UTC

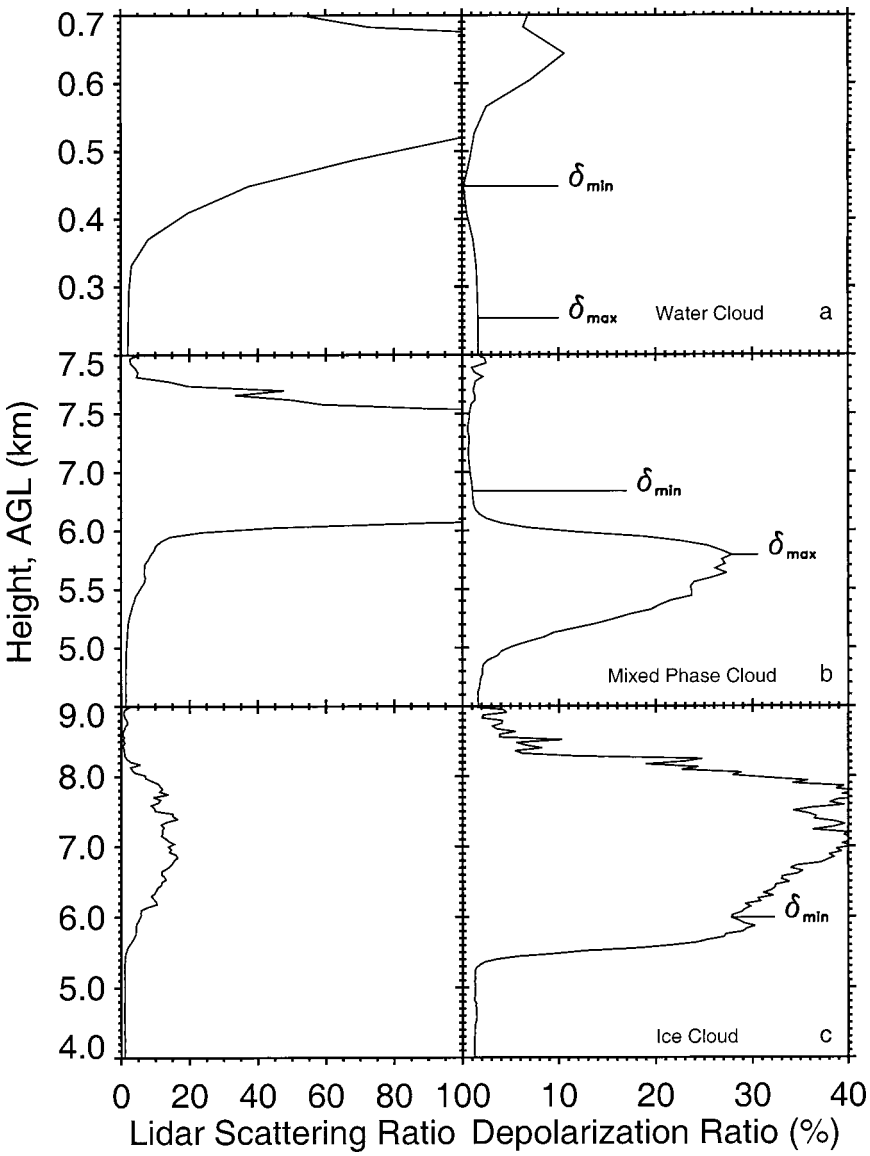

FIG. 6. The characteristic patterns in lidar scattering ratio and linear depolarization ratio profiles for clouds of different phases. AGL is the height above ground level.

dominate the lidar signal. For ice clouds, δ usually have no strong height dependence. These patterns have been observed by Sassen (1984) and simulated by Sassen et al. (1992), for example. As Fig. 6 illustrates, the profiles of lidar scattering ratio and δ for water, mixed-phase, and ice clouds from CART Raman lidar measurements display these typical patterns.

Cloud phase can be discriminated by identifying these patterns, as was used to identify supercooled liquid water clouds in Sassen and Zhao (1993) and Young et al. (2000). In our case, cloud phase is identified using the following logic. The first step is to find the local minimum of δ ($\delta_{\min}$) between the cloud base and peak signal. If $\delta_{\min}$ is greater than 10%, it is classified as an ice cloud. If $\delta_{\min}$ is less than 10%, we examine the maximum δ ($\delta_{\max}$) between the height of $\delta_{\min}$ and the cloud base minus 50 m. If $\delta_{\max}$ is approximately the δ of the molecular return ($\sim$0.02 at visible wavelengths), the cloud is classified as a water cloud. Otherwise, it is classified as a mixed-phase cloud. A possible difficulty arises from horizontally oriented plate ice crystals, which also can generate low δ and a strong backscattered signal. However, this difficulty can be avoided by tilting the laser beam a few degrees off of the zenith direction (Sassen 1991). It is important to note that the CART Raman lidar is pointed about 3°–5° from the zenith to minimize the impact of this effect.

Note that most of the cloud statistical results given below could not employ δ-based cloud-phase discrimination because of the relatively small sample of reliable

Unauthenticated | Downloaded 05/29/24 05:42 AM UTC

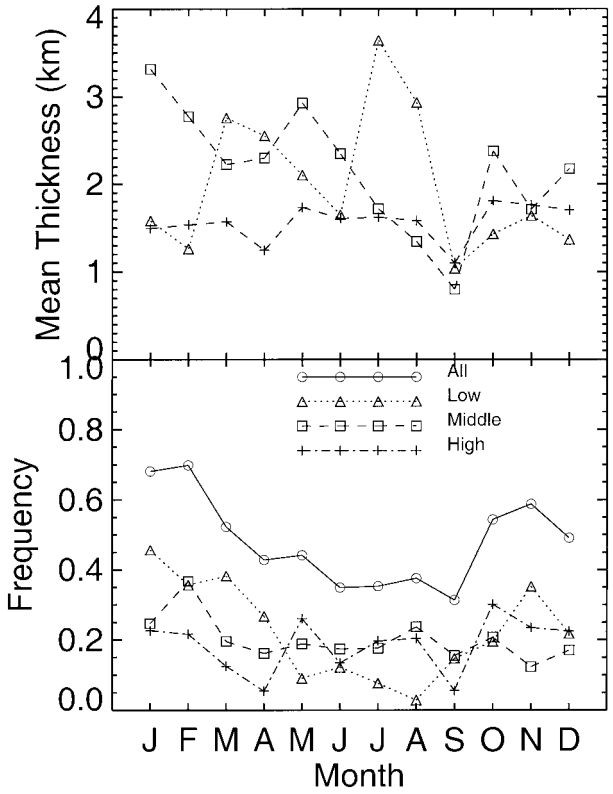

FIG. 7. Monthly cloud statistics at the SGP CART site in 1998 in terms of the mean cloud thickness and frequencies of cloud occurrence, including all clouds combined.

Raman polarization lidar data. However, the available data have been applied to characterization of mixed-phase Ac clouds to distinguish the water-dominated source cloud from the virga.

6. Cloud macrophysical properties at the ARM CART site

The algorithms discussed above are applied here to the SGP CART site observations collected during 1998. Although atmospheric conditions in this year were partly affected by the 1997–98 El Niño and 1998–99 La Niña events (Barnston et al. 1999; Mason et al. 1999), we selected this year because the Raman lidar measurements are more consistently available than in other years. Because Raman lidar data are not available for each day, MPL and ceilometer measurements are also used to generate cloud boundaries. The MWR and IR radiometer both operated together on 297 days in 1998. The statistics of cloud macrophysical properties based on 1-min data averages are presented below.

The monthly averaged frequency of cloud occurrence, which is how often a class of cloud is observed by the lidar and radar in each month, is shown in Fig. 7. In this figure, the mean cloud thickness statistics are also shown for low (base less than 2 km), middle (base between 2 and 7 km), and high clouds (base greater than 7 km). There are generally strong seasonal changes in low and middle clouds; high clouds show only smaller changes in both frequency and mean cloud thickness. Similar seasonal trends are apparent in the monthly averaged frequency of total cloud occurrence at a given height shown in Fig. 8. During the summer and early autumn, there are fewer low clouds than at other times. This figure demonstrates that significant cloud seasonal changes also occur in the vertical distribution of clouds. This strong seasonal change is a typical feature of the long-term cloud behavior at the SGP CART site (Lazarus et al. 2000).

Figure 9 depicts the yearly averaged diurnal cycle of cloud occurrence frequencies. For low cloud, there is an obvious diurnal cycle in the cloud occurrence frequency. There are more total clouds in early afternoon, due mainly to the increase in low clouds at this time. For middle and high clouds, a diurnal cycle is not apparent. The diurnal cycles of clouds for different seasons (not shown) show features similar to the yearly average.

Seasonal changes in clouds are also apparent for each cloud type, as shown in Fig. 10. As expected, there are more St in the winter and spring seasons and more convective clouds in summer and early autumn. The yearly averaged cloud type amount is compared with the ISCCP land and northern-midlatitude climatological descriptions over the 1986–93 period in Fig. 11 (Rossow and Schiffer 1999). There are obvious differences in the St and Cu occurrences between the 1998 SGP CART observations and the ISSCP data. These differences result in part from the interannual and geographic variabilities of clouds, but also result from the differences in the cloud algorithms employed. Long-term ARM-Program observations at the various sites and comparisons with satellite remote sensing data can help us to understand these discrepancies.

The yearly thickness distributions of different cloud types are provided in Fig. 12, in which obvious differences are indicated. High clouds have a maximum thickness frequency between 0.5 and 1.0 km, whereas As tend to be much thicker and cumuliform clouds tend to be thinner. For the case of Ac, cloud thickness extends to large values when virga is included in the determination of thickness. Altocumulus cloud depths are significantly reduced, however, when Raman lidar polarization data are used to ensure that the source clouds are dominated by water droplets (the dashed line in Fig. 12c). In contrast, Ns and convective cloud depths are very thick, with maximum frequencies at depths of about 8.0 km.

7. Conclusions

To improve the parameterization of clouds in GCMs and to improve our understanding of the role of clouds in the earth–atmosphere climate system, as a first step it is necessary to characterize cloud microphysical and

Unauthenticated | Downloaded 05/29/24 05:42 AM UTC

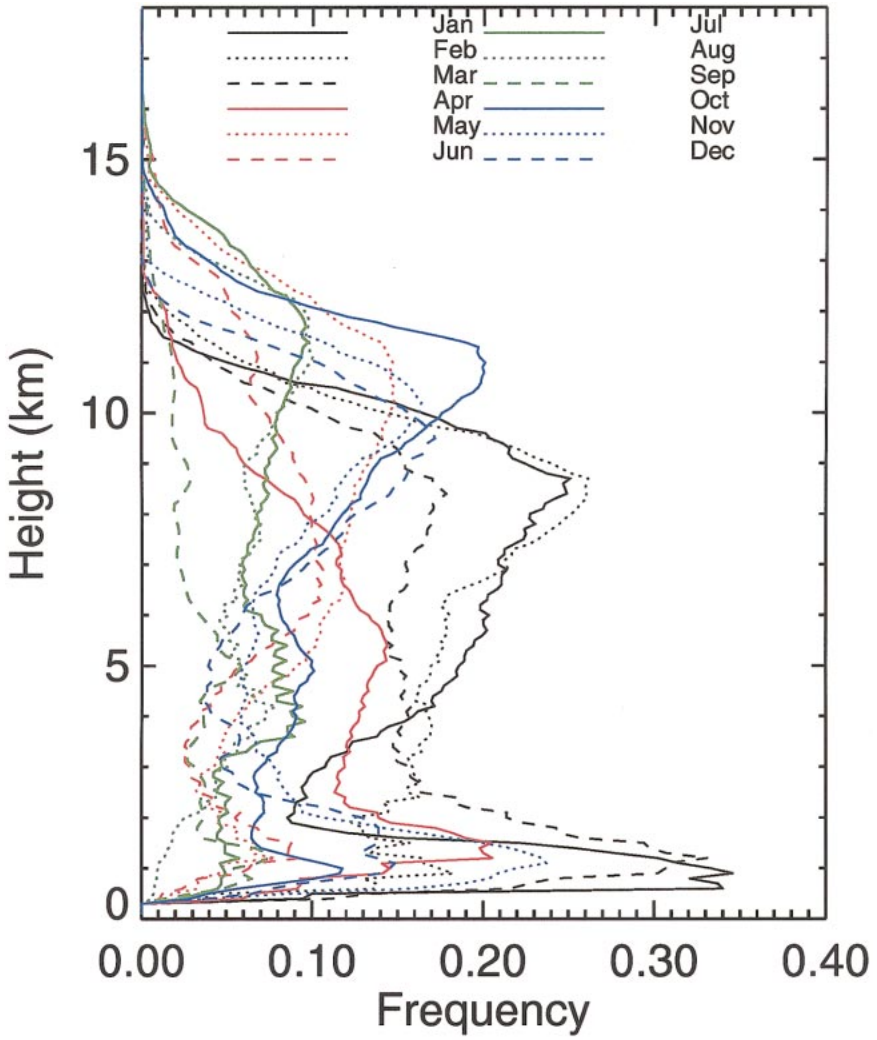

FIG. 8. The frequency of cloud occurrence of any cloud type at a given height at the SGP CART site in 1998.

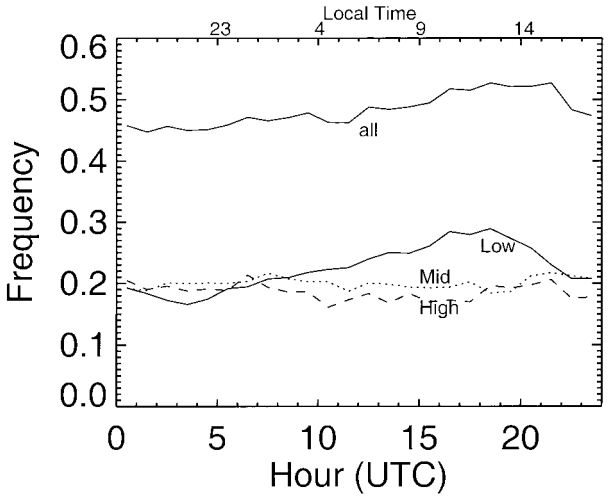

FIG. 9. The diurnal cycle of clouds at the SGP CART site in 1998.

macrophysical properties based on long-term integrated observations from surface- and satellite-based remote sensors. The ARM Program represents a major attempt to achieve this goal. In this paper, algorithms are described to derive cloud macrophysical properties using a combination of lidar, millimeter-wave radar, IR radiometer, and microwave radiometer measurements. Although these kinds of instruments are typical of modern integrated surface sites for cloud observations, note that the CART Raman lidar and the MMCR are state-of-the-art sensors that have provided us with datasets of exceptional quality. Based on our algorithm experience, however, we recommend that efforts be made to improve the accuracy and detection of small amounts of liquid water (say, less than 0.05 mm) with multichannel microwave radiometers. The unambiguous radiometric detection of such clouds would contribute to improving schemes used for liquid water cloud identification and characterization.

Unauthenticated | Downloaded 05/29/24 05:42 AM UTC

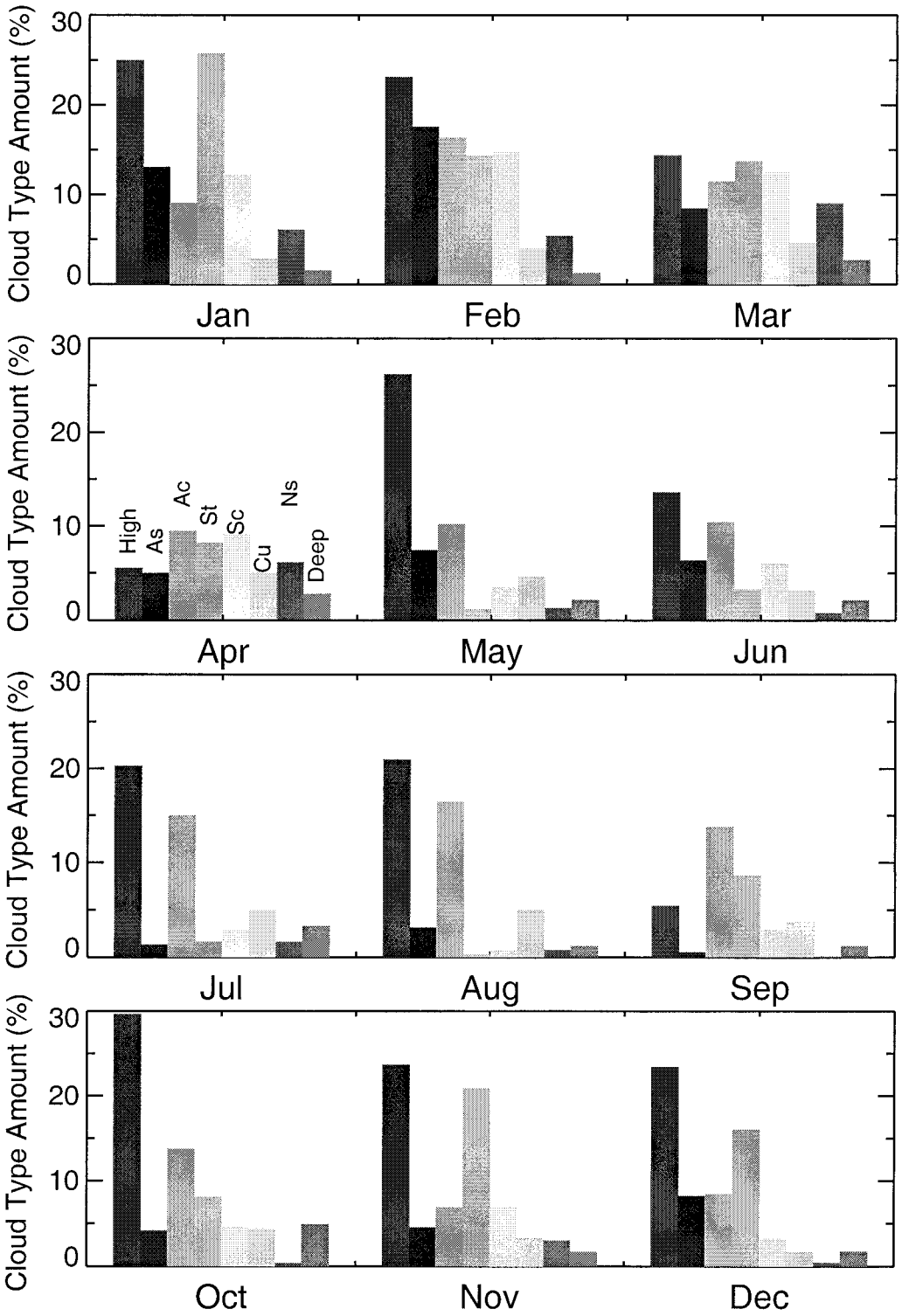

FIG. 10. Monthly cloud-amount statistics for each indicated cloud type for the 1998 SGP CART site data.

The lidar cloud-detection algorithm discussed here fully explores the information inherent in the slope of the backscattered lidar signal and introduces two physically based parameters to distinguish a cloud layer from an aerosol layer or noise: 1) the ratio of the layer peak signal to the base signal and 2) the maximum negative slope in the detected layer. This algorithm can also be applied to radar-only cloud detection with some mod-

Unauthenticated | Downloaded 05/29/24 05:42 AM UTC

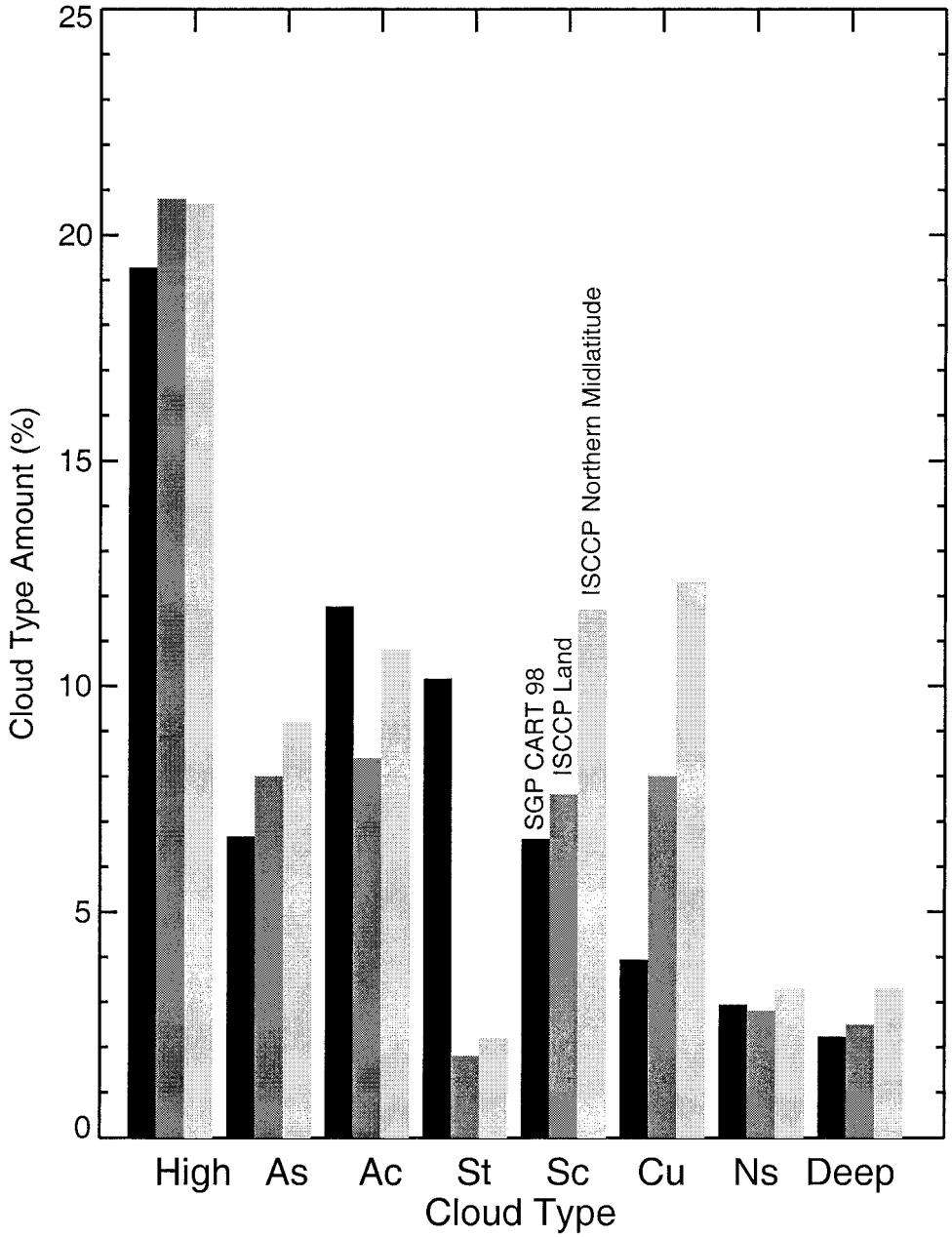

FIG. 11. Annual 1998 SGP CART cloud-amount statistics by cloud type and comparisons with the ISCCP land and northern-midlatitude datasets for 1986–93.

ifications, because the main difference between (visible wavelength) lidar and radar signals is the absence of an air return in the radar signals.

Algorithms have been presented for the study of cloud macrophysical properties, which include cloud boundaries, thickness, phase, type, and precipitation information, by combining data from four passive and active remote sensors. The different lidar and radar wavelengths complement each other, leading to the retrieval of more-reliable cloud boundaries and to better cloud detection. Cloud phase can be discriminated by identifying different patterns in the backscattered lidar signal and δ-value profiles. A cloud classification algorithm has also been proposed that classifies clouds into either St, Sc, Cu, Ns, Ac, As, deep convective, or high cloud. These algorithms have been tested and applied to the SGP CART site measurements over a full year. The resultant statistics of cloud macrophysical properties display seasonal changes in the cloud occurrence frequency, cloud type, and cloud thickness, and a notice-

Unauthenticated | Downloaded 05/29/24 05:42 AM UTC

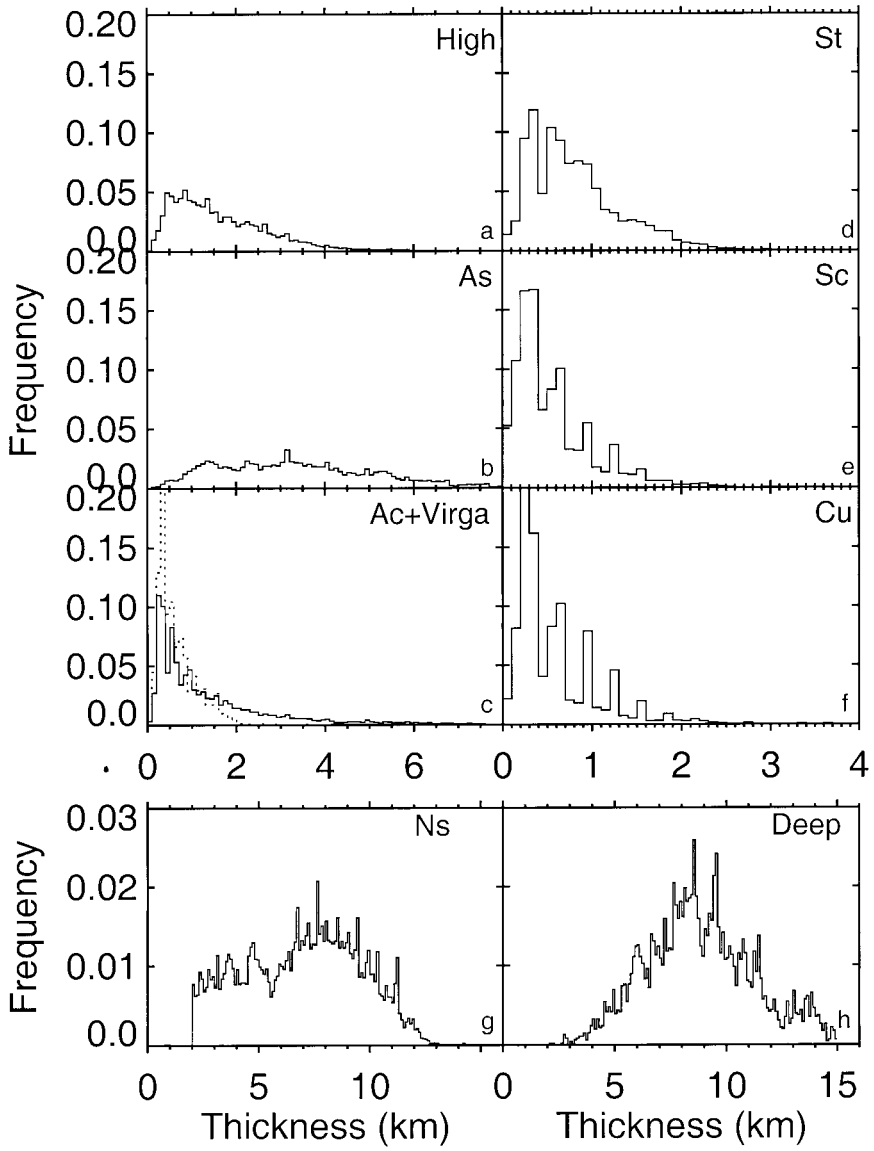

FIG. 12. Cloud-thickness distributions for different cloud types. In (c), the dashed line is for Ac derived from the polarization Raman lidar and MMCR measurements. Note the use of different cloud-thickness scales for the various cloud types.

able diurnal cycle in low clouds. This first step in compiling an advanced cloud climatological description illustrates the basic utility of the ARM remote sensing measurement program.

These algorithms are built on earlier research and represent advances in efforts to study cloud type and macrophysical properties by combining multiple remote sensors. However, we acknowledge that aspects of our approach are specific to the instruments used and the cloud studied at the SGP CART site. Although the thresholds in our lidar cloud-detection algorithm can be used under most situations, more work is needed to identify clouds in the presence of dense smoke plumes or fog. The performance of cloud-type classification schemes can be improved by finding ways to identify cloud phase under difficult situations, particularly to discriminate between highly supercooled liquid altocumulus and ice clouds. If lidar depolarization data are unavailable, alternative methods could involve combined cloud temperature and radar reflectivity data (Lohmeier et al. 1997) or further developments in the lidar signal-slope method (Sassen and Zhao 1993). The flexibility of cloud classification schemes can potentially also be improved by using more advanced methods such as fuzzy logic. To facilitate the use and further development of our algorithms by others, we plan to make

Unauthenticated | Downloaded 05/29/24 05:42 AM UTC

them available to the cloud research community via our Internet site at the University of Utah Facility for Atmospheric Remote Sensing.

Acknowledgments. This research has been supported by Department of Energy Grant DEFG0394ER61747 from the Atmospheric Radiation Measurement Program. We thank the anonymous reviewers for their comments.

REFERENCES

Asrar, G., and J. Dozier, 1994: *EOS: Science Strategy for the Earth Observing System.* American Institute of Physics, 119 pp.

Bankert, R. L., 1994: Cloud classification of AVHRR imagery in maritime regions using a probabilistic neural network. *J. Appl. Meteor.,* **33,** 909–918.

Barker, H. W., E. E. Clothiaux, T. P. Ackerman, R. T. Marchand, Z. Li, and Q. Fu, 1999: Overlapping cloud: What radars give and what models require. *Proc. Ninth ARM Science Team Meeting,* San Antonio, TX, U.S. Department of Energy. [Available online at http://www.arm.gov/docs/documents/technical/conference.html.]

Barnston, A. G., A. Leetmaa, V. E. Kousky, R. E. Livezey, E. A. O'Lenic, H. Van den Dool, A. J. Wagner, and D. A. Unger, 1999: NCEP forecasts of the El Niño of 1997–98 and its U.S. impacts. *Bull. Amer. Meteor. Soc.,* **80,** 1829–1852.

Campbell, J. R., D. L. Hlavka, J. D. Spinhirne, D. D. Turner, and C. J. Flynn, 1998: Operational cloud boundary detection and analysis from micropulse lidar data. *Proc. Eighth ARM Science Team Meeting,* Tucson, AZ, U.S. Department of Energy, 119–122.

Chen, T., W. B. Rossow, and Y. Zhang, 2000: Cloud type radiative effects from the International Satellite Cloud Climatology Project. Preprints, *11th Symp. on Global Change Studies,* Long Beach, CA, Amer. Meteor. Soc., 86–89.

Clothiaux, E. E., G. G. Mace, T. P. Ackerman, T. J. Kane, J. D. Spinhirne, and V. S. Scott, 1998: An automated algorithm for detection of hydrometer returns in micropulse lidar data. *J. Atmos. Oceanic Technol.,* **15,** 1035–1042.

——, T. P. Ackerman, G. G. Mace, K. P. Moran, R. T. Marchand, M. A. Miller, and B. E. Martner, 2000: Objective determination of cloud heights and radar reflectivities using a combination of active remote sensors at the ARM CART sites. *J. Appl. Meteor.,* **39,** 645–665.

Duchon, C. E., and M. S. O'Malley, 1999: Estimating cloud type from pyranometer observations. *J. Appl. Meteor.,* **38,** 132–141.

Eberhard, W. L., 1986: Cloud signals from lidar and rotating beam ceilometer compared with pilot ceiling. *J. Atmos. Oceanic Technol.,* **3,** 499–512.

Goldsmith, J., B. Forest, S. Bisson, and D. Turner, 1998: Turn-key Raman lidar for profiling atmospheric water vapor, clouds, and aerosols. *Appl. Opt.,* **37,** 4979–4990.

Hartmann, D. L., M. E. Ockert-Bell, and M. L. Michelsen, 1992: The effect of cloud type on Earth's energy balance: Global analysis. *J. Climate,* **5,** 1281–1304.

Lazarus, S. M., S. K. Krueger, and G. G. Mace, 2000: A cloud climatology of the southern Great Plains ARM CART site. *J. Climate,* **13,** 1762–1775.

Lohmeier, S. P., S. M. Sekelsky, J. M. Firda, G. A. Sadowy, and R. E. McIntosh, 1997: Classification of particles in stratiform clouds using the 33 and 95 GHz polarimetric cloud profiling radar system (CPRS). *IEEE Trans. Geosci. Remote Sens.,* **37,** 256–270.

Luo, G., P. A. Davis, L. L. Stowe, and E. P. McClain, 1995: A pixel-scale algorithm of cloud type, layer, and amount for AVHRR data. Part I: nighttime. *J. Atmos. Oceanic Technol.,* **12,** 1013–1037.

Mace, G. G., and K. Sassen, 2000: A constrained algorithm for retrieval of stratocumulus cloud properties using solar radiation, microwave radiometer, and millimeter cloud radar data. *J. Geophys. Res.,* **105,** 29 099–29 108.

Mason, S. J., L. Goddard, N. E. Graham, E. Yulaeva, L. Sun, and P. A. Arkin, 1999: The IRI seasonal climate prediction system and the 1997/1998 El Niño event. *Bull. Amer. Meteor. Soc.,* **80,** 1853–1873.

Moran, J. M., M. D. Morgan, and P. M. Pauley, 1997: *Meteorology: The Atmosphere and the Science of Weather.* Prentice Hall, 530 pp.

Pal, S. R., W. Steinbrecht, and A. I. Carswell, 1992: Automated method for lidar determination of cloud base height and vertical extent. *Appl. Opt.,* **31,** 1488–1494.

Parker, S. P., Ed.,1988: *Meteorology Source Book.* McGraw-Hill, 304 pp.

Penaloza, M. A., and R. M. Welch, 1996: Feature selection for classification of polar regions using a fuzzy expert system. *Remote Sens. Environ.,* **58,** 81–100.

Platt, C. M. R., and Coauthors, 1994: The Experimental Cloud Lidar Pilot Study (ECLIPS) for cloud-radiation research. *Bull. Amer. Meteor. Soc.,* **75,** 1635–1645.

Rossow, W. B., and R. A. Schiffer, 1999: Advances in understanding clouds from ISCCP. *Bull. Amer. Meteor. Soc.,* **80,** 2261–2286.

Sassen, K., 1984: Deep orographic cloud structure and composition derived from comprehensive remote sensing measurements. *J. Climate Appl. Meteor.,* **23,** 568–583.

——, 1991: The polarization lidar technique for cloud research: A review and current assessment. *Bull. Amer. Meteor. Soc.,* **72,** 1848–1866.

——, and B. S. Cho, 1992: Subvisual–thin cirrus lidar dataset for satellite verification and climatological research. *J. Appl. Meteor.,* **31,** 1275–1285.

——, and H. Zhao, 1993: Supercooled liquid water clouds in Utah winter mountain storms: Cloud-seeding implications of a remote-sensing dataset. *J. Appl. Meteor.,* **32,** 1548–1558.

——, ——, and G. C. Dodd, 1992: Simulated polarization diversity lidar returns from water and precipitating mixed phase clouds. *Appl. Opt.,* **31,** 2914–2923.

——, J. M. Comstock, Z. Wang, and G. G. Mace, 2001: Cloud and aerosol research capabilities at FARS: The Facility for Atmospheric Remote Sensing. *Bull. Amer. Meteor. Soc.,* **82,** 1119–1138.

Stokes, G. M., and S. E. Schwartz, 1994: The Atmospheric Radiation Measurement (ARM) Program: Programmatic background and design of the Cloud and Radiation Test Bed. *Bull. Amer. Meteor. Soc.,* **75,** 1201–1221.

Stubenrauch, C. J., W. B. Rossow, F. Chéruy, A. Chédin, and N. A. Scott, 1999: Clouds as seen by satellite sonders (3I) and imagers (ISCCP). Part I: Evaluation of cloud parameters. *J. Climate,* **12,** 2189–2213.

Tovinkere, V. R., M. Penaloza, A. Logar, J. Lee, R. C. Weger, T. A. Berendes, and R. M. Welch, 1993: An intercomparison of artificial intelligence approaches for polar scene identification. *J. Geophys. Res.,* **98,** 5001–5016.

Uddstrom, M. J., and W. R. Gray, 1996: Satellite cloud classification and rain-rate estimation using multispectral radiances and measures of spatial texture. *J. Appl. Meteor.,* **35,** 839–858.

Uttal, T., E. E. Clothiaux, T. P. Ackerman, J. M. Intrieri, and W. L. Eberhand, 1995: Cloud boundary statistics during FIRE II. *J. Atmos. Sci.,* **52,** 4276–4284.

Wang, P.-H., P. Minnis, M. P. McCormick, G. S. Kent, and K. M. Skeens, 1996: A 6-year climatology of cloud occurrence frequency from Stratospheric Aerosol and Gas Experiment II observations (1985–1990). *J. Geophys. Res.,* **101,** 29 407–29 429.

Wang, Z., 2000: Cloud property retrieval using combined ground-based remote sensors. Ph.D. dissertation, University of Utah, 191 pp.

Welch, R. M., S. K. Sengupta, A. K. Goroch, P. Rabindra, N. Rangaraj, and M. S. Navar, 1992: Polar cloud and surface classification

Unauthenticated | Downloaded 05/29/24 05:42 AM UTC

using AVHRR imagery: An intercomparison of methods. *J. Appl. Meteor.*, **31,** 405–420.

Williams, C. R., W. L. Ecklund, and K. S. Gage, 1995: Classification of precipitating clouds in the Tropics using 915-MHz wind profilers. *J. Atmos. Oceanic Technol.*, **12,** 996–1012.

Winker, D. M., and M. A. Vaughan, 1994: Vertical distribution of clouds over Hampton, Virginia, observed by lidar under the ECLIPS and FIRE ETO programs. *Atmos. Res.*, **34,** 117–133.

World Meteorological Organization, 1956: *International Cloud Atlas: Abridged atlas*. World Meteorological Organization, 62 pp. and 72 plates.

Young, S. A., 1995: Analysis of lidar backscatter profiles in optically thin clouds. *Appl. Opt.*, **34,** 7019–7031.

——, C. M. R. Platt, R. T. Austin, and G. R. Patterson, 2000: Optical properties and phase of some midlatitude, midlevel clouds in ECLIPS. *J. Appl. Meteor.*, **39,** 135–153.

Unauthenticated | Downloaded 05/29/24 05:42 AM UTC